Manuscript submitted to **Biophysical***Journal*

Article

Anomalous Coarsening of Coalescing Nucleoli in Human Cells

Giorgi Arsenadze , Christina M. Caragine , Taylor Coakley , Iraj Eshghi , Yuwei Yang , Alex Wofford , and Alexandra Zidovska*

Center for Soft Matter Research, Department of Physics, New York University, New York, NY 10003, USA
*Correspondence: alexandra.zidovska@nyu.edu

ABSTRACT Coarsening is a ubiquitous phenomenon in droplet systems near thermodynamic equilibrium – as an increase in droplet size lowers the system's free energy – however, coarsening of droplets in non-equilibrium systems, such as the cell nucleus, is far from understood. Liquid condensates in the cell nucleus, like nucleoli, form by liquid-liquid phase separation and play a key role in the nuclear organization. In human cells, nucleolar droplets are nucleated at the beginning of the cell cycle and coarsen with time by coalescing with each other. Upon coarsening, human nucleoli exhibit an anomalous volume distribution $P(V) \sim V^{-1}$, which cannot be explained by any existing theory. In this work, we investigate physical mechanisms behind the anomalous coarsening of human nucleoli. Using spinning disc confocal microscopy, we simultaneously record dynamical behavior of nucleoli and their surrounding chromatin prior to their coalescence in live human cells. We find that nucleolar anomalous coarsening persists during the entire cell cycle. We measure chromatin flows and density between and around nucleoli, as well as relative motion of two nucleoli before they coalesce. We find that prior to nucleolar coalescence chromatin concentration decreases in the space between nucleoli and the nucleoli move faster towards each other, resembling an effective depletion attraction between the coalescing nucleoli. Indeed, our computational simulations of nucleolar dynamics show that short-ranged attraction is sufficient to explain the observed anomalous volume distribution of human nucleoli. Overall, our results reveal a potential physical mechanism contributing to coarsening of human nucleoli. Such knowledge expands our picture of the physical behavior of liquid condensates inside the cell nucleus and our understanding of the dynamic nuclear organization.

SIGNIFICANCE Droplets near thermodynamic equilibrium are known to undergo coarsening, with an increase in droplet size lowering the system's free energy. However, coarsening of droplets in living systems, such as the cell nucleus, remains an open question. Here, we study the physical mechanism behind the anomalous coarsening of nucleoli, the largest liquid condensates found inside the cell nucleus. Using live cell microscopy, we investigate motions of nucleoli as well as flows of their surrounding genome in human cells. Taken together, our data and computational simulations reveal a potential physical mechanism contributing to coarsening of human nucleoli. Moreover, our results contribute to our understanding of the physical behavior of liquid condensates inside the cell nucleus as well as the dynamic nuclear organization.

1 INTRODUCTION

Particle coarsening – the process by which small particles become larger – has been studied across many physical and biological systems, ranging from colloids to droplets, and from protein aggregates to liquid condensates (1–3). Such studies are critical to understanding a broad set of real-world phenomena, from air and water pollution to development of diseases such as Parkinson's, Alzheimer's or type II diabetes (4–6). The kinetics of the particle coarsening, aggregation for solid particles and coalescence for liquid droplets, can vary from passive diffusion-limited process, collision-free Ostwald ripening to driven chemically-reactive coarsening (3). In particular, coarsening in thermal systems has been extensively studied with experiments, theory and simulations (7–14). The time evolution of the particle volume distribution $P(V)$, one of the principal experimental measurables, can be described by the Smoluchowski equation (15). It relates rates of particle aggregation and dissociation, yielding a characteristic scaling for the given coarsening process (3, 9, 16–18). In general, $P(V)$ is transient, as the material supply is finite. However, with a constant injection of material, volume conservation of particles pre/post coarsening and diffusive dynamics, it has been shown that the system follows the scaling solution $P(V) \sim V^{-1.5}$ (3, 17, 18).

In recent years, a plethora of droplets – liquid condensates formed by liquid-liquid phase separation – has been found inside cells (19, 20). In particular, liquid condensates, such as nucleoli and speckles, play a key role in the functional organization of the cell nucleus (21). Such liquid condensates allow the cell to spatially segregate specific molecular machinery, and hence biological processes, to specific regions of the nucleus. The biggest intracellular liquid droplet is the nucleolus, which resides inside the cell nucleus (22). The nucleolus is composed of RNA and proteins, and involved in ribosome biogenesis, cell cycle regulation as well as cellular stress response (22–24). Nucleoli form at the nucleolar organizing regions (NORs) of the genome, which contain rDNA that is transcribed within the nucleolus (25–28). Since there are 10 NORs present in the human diploid genome, human somatic cells contain 10 nucleoli at the beginning of the cell cycle (29). The nucleoli coalesce over time – leading to droplet coarsening – until they dissolve shortly before mitosis (30, 31).

The life of nucleoli is closely connected to the genome, from their nucleation at NORs to their constant immersion in chromatin solution inside the cell nucleus (21, 22). In fact, it was shown that the nucleolar surface is maintained by ATP-dependent processes such as chromatin transcription and packing, and kinetics of nucleolar coalescence is governed by the viscosity of the surrounding chromatin solution (32, 33). Additionally, the nucleolar volume distribution in human cells was found to follow $p(V) \sim V^{-1}$ (33). This differs from $P(V) \sim V^{-1.5}$ for diffusion-limited coalescence with a constant material injection, which was observed in passive droplet systems as well as for nucleoli in *X. Laevis* oocytes (3, 34). The different scaling of $P(V)$ for nucleoli in human cells suggests a deviation from a diffusion-limited behavior, hinting at a possible role of chromatin in aiding or hampering the nucleolar coalescence. Indeed, such an effect would not be surprising, as human nucleoli remain tethered to chromatin fiber during their lifetime, in contrast to nucleoli in *X. Laevis* oocytes, which are free to diffuse (35). When freely moving optogenetic droplets were introduced into human nuclei, they were found to exhibit subdiffusive dynamics due to the surrounding chromatin, with their growth following $r(t) \sim t^{0.12}$ (36). Simulations of freely moving droplets in chromatin network suggest that chromatin arrests droplet growth and coalescence, thus stabilizing the multi-droplet state (37, 38). Taken together, chromatin clearly impacts both nucleolar dynamics and kinetics of nucleolar coalescence in human cells – yet – its effect on the nucleolar coarsening remains unknown.

The goal of this work is to investigate possible physical mechanism(s) behind the anomalous nucleolar coarsening in human cells. Specifically, we examine the contributions of chromatin, its dynamics and density distribution, to the nucleolar coalescence. To this end, we measure the nucleolar coarsening as a function of the cell cycle in live human cells. Moreover, we simultaneously monitor nucleolar motions as well as dynamics and reorganization of chromatin around the nucleoli prior to their coalescence. Our data reveal that nucleolar coarsening maintains the anomalous scaling of $P(V) \sim V^{-1}$ during the entire cell cycle. We find a decrease in chromatin concentration in the space between two nucleoli before they coalesce, while at the same time the nucleoli move faster towards each other. We hypothesize that such a chromatin depletion leads to an effective attractive interaction between the nucleoli. To test this hypothesis, we perform computational simulations of nucleolar coalescence with and without an attractive interaction. We find that an effective attractive force between nucleoli can indeed lead to the anomalous nucleolar coarsening observed in experiments.

2 MATERIALS AND METHODS

2.1 Cell Culture

The stable HeLa H2B-GFP and the stable Hela H2B-GFP/NPM-mApple cell line were cultured according to ATCC recommendations (CCL-2). Cells were cultured in a humidified, 5% CO_2 (vol/vol) atmosphere at 37 °C in Gibco Dulbecco's modified eagle medium (DMEM) supplemented with 10% FBS (vol/vol), 100 units/mL penicillin, 100 μg/mL streptomycin (Invitrogen), and 4.5 μg/mL Plasmocin Prophylactic (Invivogen). Cells were mycoplasma free, as determined by the Invivogen PlasmoTest (Invivogen). For timelapse experiments, H2B-GFP cells were plated 48 h prior to experiment on 35-mm MatTek dishes with glass bottom no. 1.5 (MatTek), and transiently transfected 24 h prior to experiment with NPM-mApple plasmid (32) using Lipofectamine 2000, following product protocol (Invitrogen). For DCS experiments, H2B-GFP/NPM-mApple cells were plated 24 h prior to experiment on 35-mm MatTek dishes with glass bottom no. 1.5 (MatTek). Prior to experiments, the cell media was changed to Gibco CO_2-independent media supplemented with L-Glutamine (Invitrogen). When specified, cells were synchronized using 10 μM RO 3306 (ALEXIS), which arrests cells at the G2/M checkpoint of the cell cycle. Cells were then released 1 h before imaging by washing with CO_2-independent media supplemented with L-glutamine. Cells were mounted on the microscope stage in a custom-built environmental chamber maintained at 37 °C with 5% CO_2 supplied throughout the experiment. The nuclear and nucleolar phenotype was found identical for the NPM-mApple transfected cells and NPM-mApple stable cell line, with NPM-mApple reliably localizing to nucleoli in both cases (Fig. S1). Signal-to-noise ratio was obtained by masking the nucleoli in the NPM-mApple signal and computing the ratio of the root-mean-square signal inside and outside the nucleolar region. Due to higher signal-to-noise ratio in NPM-mApple transfected cells than in stable cell line (Fig. S1), transfected cells were used for cell-cycle long high-precision nucleolar volume measurements. We further evaluated the effect of varying NPM-mApple expression in transfected cells on the nucleolar coalescence kinetics, by comparing volume distributions of nucleoli with high and low NPM-mApple signal, finding their volume distributions to be indistinguishable (Fig. S2).

2.2 Microscopy

Cells were imaged with a Yokogawa CSU-X1 spinning disc confocal head with an internal motorized high-speed emission filter wheel, Spectral Applied Research Borealis modification for increased light throughput and illumination homogeneity on a Nikon Ti-E inverted microscope equipped with an oil-immersion 100× Plan Apo NA 1.4 objective lens, and oil-immersion 60× Plan Apo NA 1.4 objective lens, and the Perfect Focus system. The microscope was mounted on a vibration-isolation air table. The pixel size was 0.065 μm for the 100× objective and 0.1075 μm for the 60× objective. H2B-GFP and NPM-mApple was excited with a 488-nm and a 561-nm solid-state laser, respectively, and their emission was collected with a 405/488/561/640 multiband-pass dichroic mirror (Semrock) and then an ET525/50m and an ET600/50m emission filter (Chroma Technology), respectively. To image H2B-GFP and NPM-mApple at the same time, we illuminated the sample simultaneously with both excitation wavelengths, 488 and 561 nm. The emission was separated by the W-View Gemini Image Splitter (Hamamatsu) using a dichroic mirror (Chroma Technology), followed by an ET525/30m and an ET630/75m emission filter (Chroma Technology). The two fluorescent signals were allocated to the two halves of the image sensor, producing two distinct images. Images were obtained with a Hamamatsu ORCA-R2 cooled CCD camera controlled with MetaMorph 7 (Molecular Devices). The exposure time for each frame was 250 ms. The streams of 16-bit images were saved as multi-tiff stacks.

2.3 Image Processing and Data Analysis

Images were converted to single-tiff images and analyzed with MatLab (The MathWorks). The nuclear and nucleolar contours were determined from the H2B-GFP and NPM-mApple signal, respectively, using previously published procedures (32, 39). For time lapse experiments, nucleoli were manually identified and matched between frames, to follow the shape changes of individual nucleoli. Images of the cells were taken every 3 hours over a 24 hour period, resulting in a total of 8 time points starting at 3 h. The images were z-stacks with 17 focal planes, 0.5μm apart. For synchronization purposes, only cells undergoing mitosis at $t = 0$ were selected for further analysis. Nucleolar areas and minor axes were determined by considering the contour of the nucleolus in the equatorial plane of the nucleolus.

2.4 Displacement Correlation Spectroscopy (DCS)

The acquired images were analyzed using DCS following procedures described in (40). Chromatin displacement maps were calculated for $\Delta t = 0.25 - 22.5$ s for 56 HeLa nuclei using protocol in (40). DCS calculations were carried out using the New York University High Performance Computing Cluster.

2.5 Chromatin Flux Calculations

Chromatin fluxes were calculated for three regions of interest: *(i)* in the channel separating pairs of nucleoli, *(ii)* in the boundary layer surrounding each nucleolus, *(iii)* the rest of the nuclear bulk. The first region is built using the following geometric construction: the centers of the two nucleoli are identified, and a connecting line is drawn between them. Then, two lines are drawn perpendicular to the first one, one line through each of the nucleolar centers. The locations where these lines intersect the boundary of each nucleolus will be the four corners of the "channel" region of interest. In the case of the "channel" geometry between two nucleoli, the chromatin displacements and velocities are then decomposed into a coordinate system which is determined by the relative positions of the nucleoli. The two components of chromatin displacements and velocities are denoted "parallel" and "perpendicular". The "parallel" coordinate axis is defined by the line connecting the centroids of the two nucleoli, and the "perpendicular" coordinate axis is perpendicular to it, and thus pointing along the channel between the two nucleoli. The construction of the boundary layer region of interest is as follows: The mask of the nucleolus is dilated by 5 pixels, and the difference between the original and dilated mask is defined as the boundary layer. Finally, the bulk region is defined by taking the whole nucleus, removing the masks of the nucleoli and the channel as defined above, and eroding the boundary layer by 10 pixels to avoid effects from the nuclear envelope.

2.6 Nucleolar Volume Measurements

The volumes of nucleoli were calculated using two different methods: *(i)* spherical approximation and *(ii)* trapezoidal rule, to verify the results. For both methods, the input data are z-stacks of NPM-mApple images with planes 0.5 μm apart. The first method was used in (33), it uses the image from the z-stacks, which contains the equatorial plane of the nucleolus and obtains nucleolar contour as well as area A delineated by the contour in this plane. Next, the nucleolar volume is estimated by assuming a spherical shape, with $V = \frac{4}{3}\pi\,(A/\pi)^{3/2}$. The second method uses the entire z-stacks of confocal images and nucleolar contours in each plane. The nucleolar volume is then approximated using a trapezoidal rule (41) to estimate the integral

$$V = \int A(z)dz \approx \Delta z \left(\frac{A_1 + A_N}{2} + \sum_{i=2}^{N-1} A_i \right) , \qquad (1)$$

where N is the number of focal planes, A_i are the nucleolar areas in each plane for the given nucleolus and $\Delta z = 0.5$ μm is the spacing between the planes in the z-stack. The accuracy of the two methods was tested by fitting an example nucleolus to an ellipsoid, and comparing the two estimated volumes to the best-fit ellipsoid volume. The spherical method had an error ~ 5%, while the trapezoidal method led to an error ~ 2%. However, the resulting scaling form of the nucleolar volume distributions remains unaffected, with the $P \sim V^{-1}$ scaling recovered in both cases (Fig. S3). In this paper the results presented use the trapezoidal method, due to overall higher precision of this approach.

2.7 Simulations

We perform simulations of droplet coalescence to investigate distributions of droplet volumes under different environmental and physical conditions. The droplets, which represent nucleoli, are initialized in a simulation box with periodic boundary conditions. The side length L of the cubic box is chosen such that the initial volume fraction of droplets is $\phi = 0.05$, matching the works (34, 36, 42), with initial droplet volumes uniformly distributed between $0.5 - 1.5$ and the initial number of droplets being a parameter of the simulation. The time evolution of the droplets was done using fractional Gaussian noise, generated using the freely available code FFGN (43). The method generates fractional Gaussian walks of desired length and Hurst parameter, based on the circulant embedding method for persistent noise. This results in a fractional noise process with the exact desired autocovariance (44).

In our simulations, we explore the following regimes of behavior: *(i)* We simulate particles with no interactions and constant (or no) injection of new droplets, following the work in (34). *(ii)* The second regime is characterized by attractive forces between the droplets, with and without injection of new droplets. For regime *(i)*, after every coalescence if the resulting droplet is larger than a prescribed fraction of the box size, it is reduced in size back to a radius of 1, to prevent any single drop from taking up too much space in the box. For regime *(ii)*, once droplets are too large they are removed from the simulation. In each case, the data were collected over 100 parallel simulations with 10 initial droplets. Further details of simulation parameters are reviewed in *Supplemental Information*.

In the case of attractive interactions between nucleoli (regime *ii*), the droplets are initialized at random locations in the box and evolved using FFGN for the desired number of time steps, with an added deterministic drift which is generated by the prescribed pairwise force field. The latter can be chosen to decay as a power-law or an exponential, and has a hard cutoff to prevent excessive slowing down of the code due to pairwise calculation of far-off forces. At every time point, the code checks whether two droplets overlap. If so, those droplets fuse, becoming one droplet with volume equal to the sum of its parent droplets, and a center localized at the average of the previous two droplet positions. It inherits the random walk of one of its parents (these are generated at the start of the simulation), chosen at random. After the system has evolved for the prescribed number of steps, the resulting volume distribution is binned into a log-histogram and fit to a power-law.

2.8 Statistical Analysis

The statistical significance of the reported results was evaluated using the following tests and assessments: Significance of correlations was evaluated using Pearson correlation coefficients as implemented in the `corrcoef()` function in MATLAB. Where error bars are shown as shaded regions, they correspond to the standard error. To assess statistical significance of measured differences among *MSD* curves, a reduced χ^2-test was used.

3 RESULTS

3.1 Nucleolar Volume Distributions During the Cell Cycle

To elucidate the role of chromatin in the nucleolar coarsening, we first measure volumes of nucleoli in live cells as a function of the cell cycle progression. To this end, we use HeLa cells with fluorescently labeled chromatin (H2B-GFP) and nucleoli (NPM-mApple), which we synchronize at the beginning of their cell cycle. Using spinning disc confocal microscopy, we follow cells that were mitotic at $t = 0$ h and record high-resolution z-stacks of images of these cells every 3 h over the course of 24 h.

Figure 1A shows a series of micrographs of nuclei at 10 different timepoints during the cell cycle, with mitosis being $t = 0$ h. Over the course of 24 h, we see the number of nucleoli decrease as they progressively coalesce into larger droplets. Since the first time point at which we evaluate nucleolar volume is $t = 3$h, we do not expect to observe 10 nucleoli as by then some may have already coalesced (Fig. S4). An enlarged view of two examples of nuclei containing nucleoli undergoing coalescence is shown in Fig. 1B. At each timepoint, we collect a z-stack of images in 17 focal planes 0.5 μm apart, allowing us to visualize the entire 3D organization of the nucleus. For each nucleolus we obtain a contour from the NPM-mApple signal using established methods (32). We collect a nucleolar contour at every focal plane and every timepoint, where the given nucleolus is present in

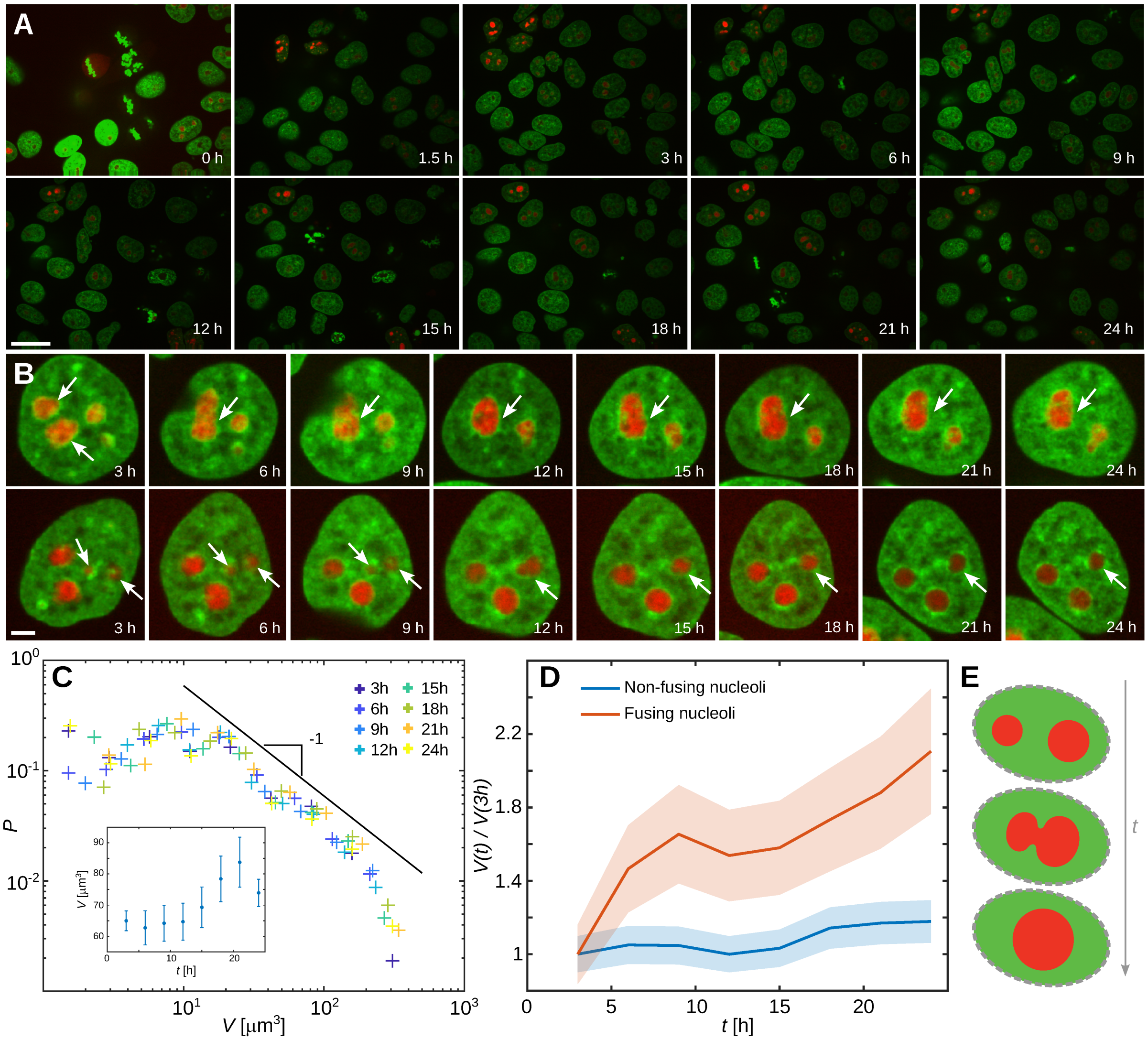

Figure 1: Coarsening of nucleoli in human cells follows anomalous volume distribution. (*A*) Micrographs of HeLa cells with fluorescently labeled chromatin (*green*) and nucleoli (*red*) during the cell cycle. Cells were synchronized to undergo mitosis at $t = 0$ h. Nucleoli are observed to coarsen over time. Scale bar, 25 μm. (*B*) Micrographs of two nucleolar coalescence events. Nucleoli approaching each other and coalescing are highlighted by white arrows. Scale bar, 3μm. (*C*) Distribution of nucleolar volumes calculated using trapezoidal rule for 8 time points during the cell cycle. Solid line indicates characteristic scaling of volume probabilities $p(V) \sim V^{-1}$. Nucleoloar volume was measured for 141 nucleoli across 35 cells. Inset shows mean and standard error of the volumes as a function of time. (*D*) Average volume of fusing and non-fusing nucleoli as a function of the cell cycle. The volumes are normalized by their value at 3h. Nucleoli are identified as fusing ($N = 38$) and non-fusing ($N = 103$), based on whether they fuse or not during the 24 h observation. Shaded regions indicate SE. (*E*) Schematics of nucleolar droplet coalescence with time. Nucleoli are shown in red and chromatin in green. Images in (*A*) and (*B*) correspond to single focal planes.

the data. To compute nucleolar volume from this data, we use two different methods: *(i)* Using the spherical approximation following (33), where we estimate the nucleolar volume from the area in the equatorial plane, assuming nucleolus is a sphere. *(ii)* Using the trapezoid rule and using information about the nucleolus in 3D from the z-stack. To this end, we integrate the area obtained from nucleolar contours across all focal planes using the trapezoidal rule (41). Both methods yield comparable results, with the latter method having a slightly higher precision (for comparison see *Materials and Methods*, Section 2.6 and Fig. S3). Figure 1C shows the nucleolar volume distributions (from trapezoidal rule) measured for 8 different time points in the cell cycle. The lower bound of the measured volumes is given by our high-precision method for nucleolar volume measurements (s. *Materials and Methods, Section 2.6*), which requires nucleoli to be above a certain size ($\sim 1 \mu m^3$), while the upper bound is set by the nuclear size ($\sim 10^3 \mu m^3$). We fit each of these volume distributions to a power-law (fitting range $10 - 500$ μm^3). We find that all of them scale as $P(V) \sim V^{-1}$ (Fig. S5), which is in agreement with our earlier study (33).

The scaling of the volume distribution $P(V)$ of a statistical ensemble directly informs on its coarsening mechanism (3, 9, 16–18). Strikingly, the scaling we observe for human nucleoli differs from the scaling of nucleolar volume distributions in *X. Laevis* oocyte, which follow $P(V) \sim V^{-1.5}$ (34), indicating a different coarsening process. Furthermore, the power-law dependence $P(V) \sim V^{-1}$ seems to remain consistent throughout the different times in the cell cycle, despite the ongoing coarsening, i.e., volume distributions at later times contain more larger nucleoli. Indeed, at $t = 3$h, we observe 141 nucleoli in 35 cells, while by $t = 24$h the number of nucleoli decreases to 119. It is important to note that since we do not analyze nucleoli below a certain size, the number of coalescence events we observe is only a lower bound.

To assess the effect of nucleolar coalescence vs. other potential coarsening mechanisms, such as the Ostwald ripening, we measure changes in the average volume of the fusing and non-fusing nucleoli during the cell cycle (Fig. 1D). Since we only measure the volume of larger nucleoli (due to our high-precision volume measurement), we anticipate an increase in their volume in case of the Ostwald ripening. However, we find that non-fusing nucleoli do not change their volume significantly over the first 15 hours, while fusing nucleoli show a strong volume change. The volume scaling of $p(V) \sim V^{-1}$ is maintained during these 15 hours dominated by coalescence events. At times 15–24 hours, the volume of nonfusing nucleoli slightly increases ($\sim$ 15%), however, the volume scaling of -1 remains preserved. Importantly, the volume distribution of non-fusing nucleoli from Fig. 1D also follows $P(V) \sim V^{-1}$ (Fig. S6), suggesting that these larger nucleoli were themselves formed by coalescence of smaller nucleoli early in the cell cycle.

Taken together, our evidence suggests that the coalescence remains the dominating effect on the nucleolar volume distribution. Thus, while we do not rule out a presence of the Ostwald ripening in the system, our data suggests the coalescence is the dominating coarsening mechanism. A schematic of the droplet coalescence is shown in Fig. 1E, where we illustrate two droplets (*red*) coming together, forming a neck upon contact (as seen in Fig. 1B), before fusing into one larger droplet with a volume equal to the sum of its parent droplets. Interestingly, the observed $P(V) \sim V^{-1}$ distribution as well as its mean are divergent, if integrated over all volumes from 0 to ∞. However, if measured within finite bounds given by the experiment, e.g. maximum nucleolar volume is limited by the volume of the nucleus, the mean can be obtained. In addition, the mean of the volume distribution increases throughout the cell cycle (Fig. 1C, inset), which is a known characteristic of coalescence processes (11).

3.2 Chromatin Fluxes Between Coalescing Nucleoli

To elucidate the anomalous scaling of the measured volume distribution of nucleoli in human cells, we investigate the role of chromatin in the process of the nucleolar coalescence. To this end, we measure the flux of chromatin in the space between two nucleoli on short timescales ($\sim$ seconds). We record 25 s streams of images with temporal resolution of 250 ms of 38 HeLa cell nuclei, containing 43 pairs of nucleoli. Fig. 2A-B shows an example of such a nucleus with micrographs of H2B-GFP and NPM-mApple signals, respectively. From the H2B-GFP signal, we obtain maps of chromatin displacements across the entire nucleus using Displacement Correlation Spectroscopy (DCS)(40). Figure 2C shows chromatin displacements computed at $\Delta t = 10$s. It is worth noting that this timescale is much shorter than the timescale of the coalescence itself, as we are seeking to understand the forces driving the approach of nucleoli to one another before coalescence, as opposed to the forces driving the coalescence itself.

Next, we developed a routine, which constructs a box between the two nucleoli, encapsulating the channel formed by the nucleolar boundaries. First, a line connecting centroids of the two nucleoli is drawn, followed by two lines perpendicular to the first, each of them passing through one of the centroids. The corners of the box are defined as the points, where latter intersect with the nucleolar contour. If there are multiple intersections with the nucleolar contour, we select the one that is closest to the other nucleolus. In such case, the edges of the box do not coincide with the diameter of the nucleoli, as seen in Fig. 2D-E and Fig. 3D . The resulting polygon is shown in blue in Fig. 2D-E. We then analyze the chromatin displacements within this region of interest (Fig. 2F). Specifically, we use the blue polygon as a mask, which we apply to measured chromatin displacement maps. It is important to note that that since nucleolar radii are $\sim 1\mu$m and the height of the confocal volume is $\Delta z = 0.5\mu m$, some chromatin flows although measured in between nucleoli can appear to be inside the nucleolus (Fig. 2F), when in reality they are above and below the nucleolus, but below our z-resolution.

To analyze the chromatin fluxes, we first define the key variables as illustrated in Fig. 2G: the minor axis of the smaller nucleolus, l_{min}, the distance between the nucleolar centers, d_{center}, the minimum distance between the surfaces of the two nucleoli d, and the coordinate system for the "parallel" and "perpendicular" components of the chromatin displacements, $\vec{v}_{\parallel}$ and $\vec{v}_{\perp}$. We then calculate the chromatin velocities separated into a local coordinate system shown in Fig. 2E–G, where the velocities are separated into a component down the channel $\vec{v}_{\perp}$, and another going across the channel $\vec{v}_{\parallel}$. Next, we temporally average $\vec{v}_{\parallel}$ and $\vec{v}_{\perp}$ within the region of interest (see *Materials and Methods*, Section 2.5) defined by the blue polygon in Fig. 2D-E. Fig. 2H shows the distribution of chromatin velocities in the channel between pairs of nucleoli, as measured by DCS for $\Delta t = 10$ s. We find that the velocity component down the channel ($v_{\perp}$) is Gaussian-distributed. However, the velocities across

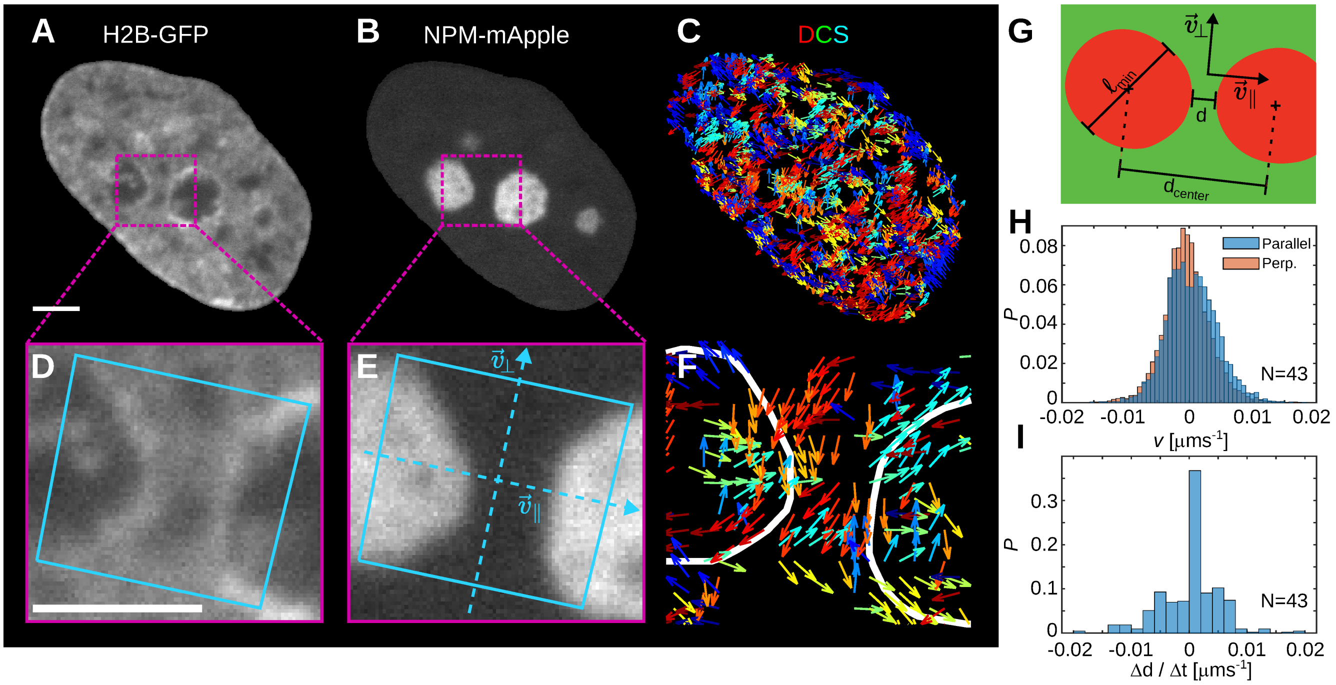

Figure 2: Chromatin flows in the space between nucleoli. Micrograph of a HeLa cell nucleus, with fluorescently labeled (*A*) chromatin (H2B-GFP) and (*B*) nucleoli (NPM-mApple). (*C*) Map of chromatin displacements measured by DCS across the nucleus shown in *A*–*B*. Displacement vectors are color-coded by their direction. (*D*) and (*E*) Enlarged images of the insets in (*A*) and (*B*), respectively. Blue box indicates the automatically-generated region of interest for analysis of chromatin fluxes between the nucleoli. Blue dashed arrows indicate directions for parallel and perpendicular components of chromatin fluxes within the channel between two nucleoli. (*F*) Chromatin displacement map for region shown in (*D*–*E*). (*G*) Diagram of two nucleoli indicating key variables: l_{min} is the minor axis length of the smaller of the two nucleoli, d_{center} is the distance between the centers of the nucleoli, d is the minimal distance between nucleolar boundaries, and $v_\parallel$, $v_\perp$ indicate the components of the velocity field in the coordinate system generated by the channel between the two nucleoli shown in (*E*). (*H*) Distributions of $v_\perp$ and $v_\parallel$ in the channel between two nucleoli given by polygon from (*E*), measured over 43 nucleolar pairs by DCS at $\Delta t = 10$ s. (*I*) Distribution of relative nucleolar velocities $\Delta d/\Delta t$ with respect to each other for $\Delta t = 10$ s. Scale bars, $3\mu m$.

the channel ($v_\parallel$) exhibit a dip at small values, deviating from Gaussian behavior. This is in contrast to the data in the bulk (Fig. S7), where both $v_\parallel$ and $v_\perp$ are Gaussian-distributed. To compare the chromatin velocities against the nucleolar velocities, we calculate the relative velocity of the nucleolar boundaries moving with respect to each other, by calculating their minimal distance as a function of time $d(t)$ and from it computing the nucleolar velocity for a time lag $\Delta t = 10$ s, matching our DCS data. These relative velocities are shown in Fig. 2I, with their magnitudes being in good agreement with chromatin velocities in Fig. 2H. Moreover, Fig. 2I shows that the distance between two nucleoli exhibits significant fluctuations over $\Delta t = 10$ s. Distribution of d at $t = 0$ and measurements of $d(t)$ are shown in Fig. S8. Our data suggests that the motion of the nucleoli, as well as their close proximity, may contribute to the unusual shape of the distribution of $v_\parallel$ in the space between the nucleoli (Fig. 2H). We perform the same velocity analysis also for shorter timescales $\Delta t = 0.25$ s (Fig. S9) and find that distributions of all chromatin and nucleolar velocities behave like a Gaussian, with relative nucleolar velocity having no bias in either direction. Velocity magnitudes are larger at these shorter timescales, consistent with earlier observations (33, 40). It is important to note that the cell nucleus is a non-equilibrium system, with nucleoli being immersed in an active polymeric chromatin fluid, which is known to exhibit strikingly different dynamical behavior than a simple viscous fluid (21, 40, 45, 46).

We also calculate the fluxes of chromatin through the channel as a function of time, and find that the resulting averages change roughly linearly with time, as shown in Fig. S10A-B. From linear fits to this data, we then extract the temporal rates of the velocities $|\partial_t v_\perp|$ and $|\partial_t v_\parallel|$, which we review as a function of normalized distance d_{center}/l_{min}, Fig. S10C and Fig. S10D, respectively. Interestingly, $|\partial_t v_\perp|$ is strongly correlated with the distance between the nucleoli (Pearson coefficient ~ 0.6), while $|\partial_t v_\parallel|$ shows no significant dependence (Pearson coefficient~ 0.09). This suggests that the net chromatin flow rate through the nucleolar channel may be affected by the proximity of the two nucleoli to each another. This motivates us to further examine chromatin within the space between two nucleoli, in particular we focus on the chromatin's spatial distribution and its changes prior to the nucleolar coalescence.

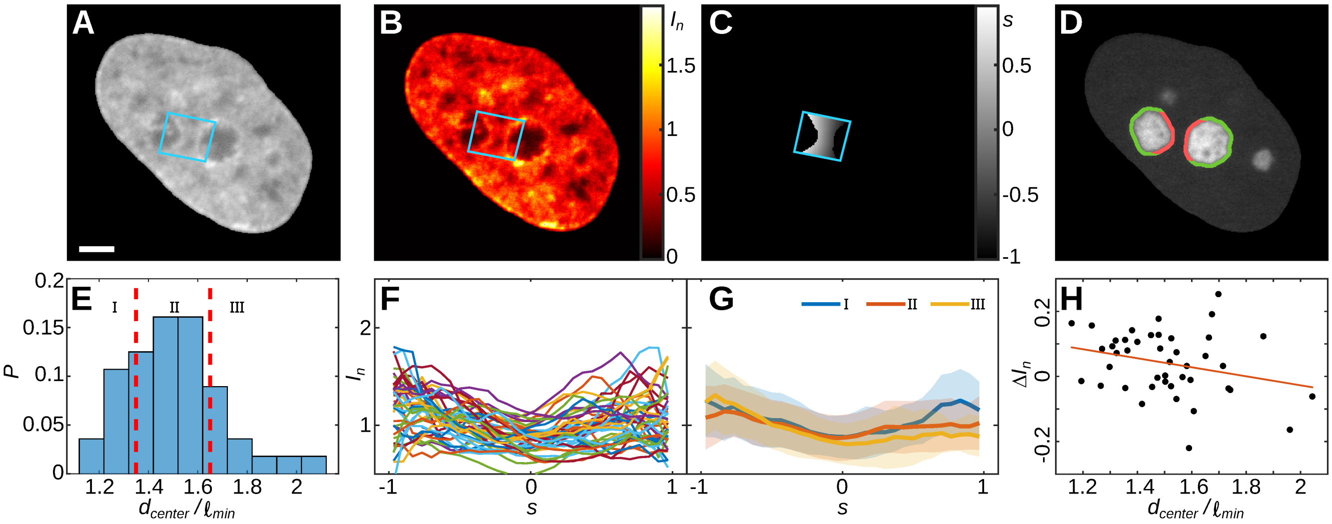

Figure 3: Chromatin density in the space between two nucleoli. (*A*) Micrograph of a cell nucleus with fluorescently labeled chromatin (H2B-GFP). Cyan polygon indicates the same box shown in Fig. 2D–E. (*B*) False-color image of nucleus from *A* indicating the local chromatin compaction I_n. (*C*) Relative distance s in the channel between nucleoli. (*D*) Micrograph of the cell nucleus from *A* with fluorescently labeled nucleoli (NPM-mApple). Nucleolar contour is color-coded by *pink* and *green* indicating the "inner" and "outer" region, respectively. (*E*) Distribution of normalized distances between nucleoli, given by d_{center}/l_{min}, with d_{center} the distance between the centroids of the two nucleoli and l_{min} minor axis of the smaller nucleolus. (*F*) Chromatin density profile in the channel between two nucleoli measured by I_n and plotted as a function of relative distance s. (*G*) Average density profiles, grouped by distances between nucleoli. The groups are indicated by the red dashed lines in histogram in (*E*). (*H*) Difference in the chromatin density in the outer vs. inner regions indicated in (*D*), plotted as a function of normalized distance d_{center}/l_{min}. The line in red shows the best linear fit to the data. The Pearson correlation coefficient between ΔI_n and d_{center}/l_{min} is -0.28. We analyzed 43 nucleolar pairs across 38 cells. Scale bar, 3μm.

3.3 Nucleolar Coalescence and Density of the Surrounding Chromatin

Chromatin density distribution between and around nucleoli will likely affect the nucleolar coalescence. Indeeed, nucleoli are decorated with a dense heterochromatin layer on their surface and chromatin is thought to be involved in maintaining the nucleolus-nucleoplasm interface (33, 47, 48). We hypothesize that chromatin density between two nucleoli may change prior to the nucleolar coalescence, since a dense chromatin layer on the nucleolar surface would physically prevent the droplets from touching and coalescing. Therefore, next we measure changes in chromatin density in the space between two nucleoli before they coalesce.

First, we measure the H2B-GFP intensity, which is a reliable proxy of chromatin density (49), for every pixel across the entire nucleus (Fig. 3A). Next, we define a local chromatin compaction I_n, which corresponds to a normalized H2B-GFP intensity and thus accounts for the cell-to-cell variability in the H2B-GFP expression (46). Specifically, $I_n = \frac{I-I_{min}}{\langle I \rangle}$, where I is the H2B-GFP intensity at the given pixel, I_{min} is the minimum pixel intensity in that nucleus, and $\langle I \rangle$ is the average intensity in the given nucleus. Fig. 3B shows I_n plotted for every pixel of the nucleus from Fig. 3A.

Next, we analyze the chromatin compaction I_n between two nucleoli. To this end, we calculate the chromatin compaction profile between two nucleoli using the normalized relative distance s, as shown in Fig. 3C. s is calculated by taking the distance from the pixel of interest to the smaller of the two nucleoli, and subtracting the distance to the larger nucleolus, and re-scaling it so that $s \in [-1, 1]$. An example is shown in Fig. 3C. We also define two characteristic regions on the nucleolar contour, the inner and outer, shown in pink and green color, respectively, in Fig. 3D. In addition, we group the studied nucleolar pairs into three populations defined by their normalized internuclear distance d_{center}/l_{min} as shown in Fig. 3E. Groups I, II, and III contain $9, 24$, and 9 nucleoli, respectively. The groups were identified by visual inspection of the distribution, with the goal to separately consider the tails of the distributions towards small and large values of d_{center}/l_{min}. As the distribution peaks strongly around its mode, group II has more members than the others. Next, we collect the I_n values across the grid of s for all pairs of nucleoli. Fig. 3F displays chromatin compaction profiles for all nucleolar pairs, while Fig. 3G shows the average compaction profiles for the three populations of nucleolar pairs (groups I, II and III). These profiles exhibit peaks near the chromatin boundaries at $s = \pm 1$, as expected due to the presence of the heterochromatin layer at the chromatin surface. However, the shape of these profile does not change significantly among the three nucleolar populations.

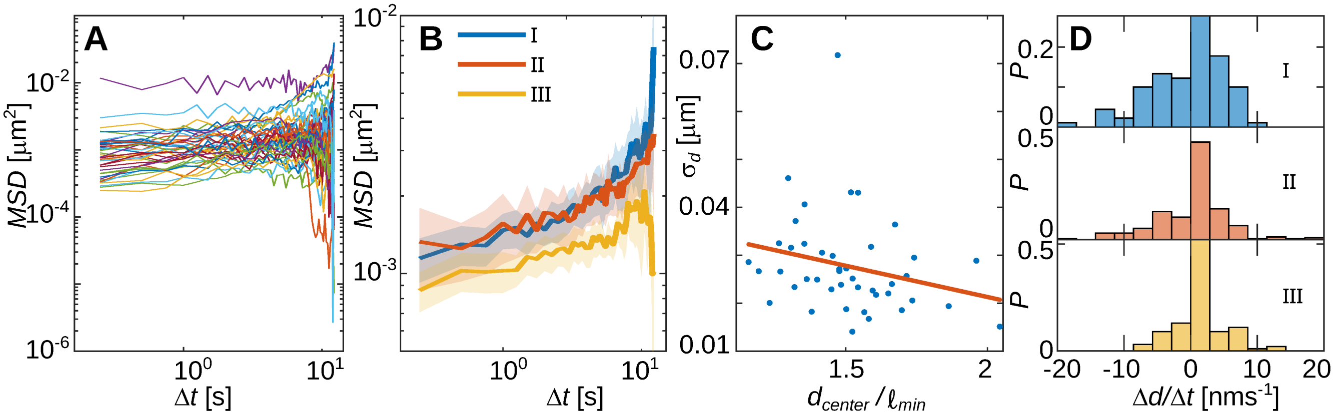

Figure 4: Mobility of nucleoli increases with their proximity to each other. (*A*) Mean squared displacements (*MSDs*) of d for 43 pairs of nucleoli across 38 cells. *MSDs* show a large range of displacements at short times. (*B*) Average *MSD*s for 3 groups of nucleolar pairs sorted by d_{center}/l_{min}. The 3 groups are defined by the bins in Fig. 3E. The *MSD* of nucleolar pairs with nucleoli closer to each other (groups I and II) increases faster with time than that of nucleolar pairs with nucleoli further apart (group III) (p-value = 0.03 between groups II and III, and $\sim 10^{-4}$ between groups I and III). (*C*) Variance σ_d of droplet separation distances d as a function of normalized distance d_{center}/l_{min}, showing a negative correlation (Pearson coefficient = -0.25). d is the shortest distance between the boundaries of two nucleoli. The line in red shows the best linear fit to the data. (*D*) Distributions of relative nucleolar velocities for groups I, II and III, at $\Delta t = 10$s (cumulative distribution over all 3 groups shown in Fig. 2I). Group I shows a statistically significant bias towards negative values (p-value of 3×10^{-3}, Fig. S12).

Further, we analyze the chromatin density along the nucleolar boundary and its change with d_{center}/l_{min}. Namely, we measure I_n for the regions of nucleolar surface defined as "inner" and "outer" (pink and green regions in Fig. 3D). These two regions are also defined by the polygon constructed in Fig. 2D–E. For each nucleolus, we compute mean I_n for both regions by averaging I_n values over all pixels in given region, and then calculate ΔI_n, which corresponds to the difference between the two means. We find that ΔI_n is negatively correlated with d_{center}/l_{min} (Fig. 3H, (Pearson coefficient of -0.28). This suggests that nucleoli far away from each other have comparable chromatin compaction along their surface in both the "inner" and "outer" region, in other words, their surface heterochromatin layer is largely of the same density around the entire nucleolus. However, as nucleoli get closer to each other, heterochromatin in the "inner" region undergoes a gradual depletion. This may effectively lead to a difference in chromatin concentrations, and thus osmotic pressure, between and around nucleoli, with higher osmotic pressure in the "outer" region. Hence, the chromatin depletion between the nucleoli may affect the nucleolar motion towards each other.

Our observations closely resemble *depletion attraction*, a well-known phenomenon in multicomponent systems (50–52). It occurs in systems containing both large and small particles, and has a thermodynamic origin. When large particles are close to each other and concentration of small particles decreases in the space between large particles, the osmotic pressure between large particles is reduced, leading to an attraction between the large particles (50). The primary signature of the depletion attraction is the density decrease of the depleted molecule between the larger particles, which is in agreement with our observations of chromatin being depleted in the space between nucleoli. These findings are congruent with those of chromatin flows in Fig. 2. The local heterochromatin decondensation is consistent with our observation of slightly higher $v_{\|}$ (Fig. 2H). Moreover, when nucleoli are farther apart, chromatin experiences bigger changes in its velocity (Fig. S10D), and the chromatin density is more homogeneous around the nucleolus (smaller ΔI_n, Fig. 3H). This suggests that as the nucleoli come closer together and ΔI_n increases (i.e. the attractive force increases), the velocity rate (i.e. changes in velocity) decreases, with nucleoli moving more smoothly towards each other. In other words, as nucleoli come closer towards each other, they start to constrain the chromatin flows between them, with the flows becoming smoother. Next, we will examine the effect of chromatin depletion between nucleoli on the nucleolar motion towards each other.

3.4 Dynamics of Nucleolar Pairs

To investigate the effect of chromatin depletion between two nucleoli on their dynamics, we analyze motions of both nucleoli in each nucleolar pair. For each nucleolar pair we calculate the relative displacements of the two nucleoli over 25 s. Specifically, at each time point we determine the nucleolar contours for both nucleoli and find the minimum distance between the two contours, yielding a sequence of distances $d(t)$. Next, we calculate the mean squared displacement $MSD(\Delta t) = \left\langle (d(t+\Delta t) - d(t))^2 \right\rangle_t$, where $\langle\rangle_t$ indicates an average over all time points. This quantity informs on the motion of nucleoli relative to each another. Fig. 4A shows *MSDs* for all studied pairs of nucleoli. Following the definition of 3 nucleolar groups in Fig. 3E, we sort the measured *MSDs* into groups I, II and III by d_{center}/l_{min} and compute an average *MSD* for each group. As shown in Fig. 4B, the relative nucleolar mobility increases as they come closer to each other. The *MSD* magnitudes for group III (yellow curve in Fig. 4B) are much smaller than *MSD* magnitudes for groups I and II at all observed times. We find p-value = 0.03 between groups II and III, and $\sim 10^{-4}$ between groups I and III, suggesting that the dynamics of nucleoli in closer proximity to each other is significantly different (see Fig. S11 for $p-$value as a function of number of included datapoints). This dynamical difference between group III and others may be related to earlier observations of nucleoli exhibiting correlated motions immediately prior to their coalescence (33).

We find that the magnitude of the relative nucleolar displacements in Fig. 4A varies among different nucleolar pairs. We evaluate these differences quantitatively by computing the standard deviation σ_d of the measured distances $d(t)$ of all nucleolar pairs. The values of the nucleolar distances at $t = 0$ s and their subsequent fluctuations over time are shown in Fig. S8. When surveying σ_d as function of the normalized nucleolar distance d_{center}/l_{min}, we find they are correlated (Fig. 4C, Pearson coefficient of -0.25), indicating an increase in nucleolar mobility as they come closer to one another.

Finally, we evaluate the fluctuations of the intranucleolar distance for the 3 groups. To this end, we compute the distributions of relative nucleolar velocities $\Delta d/\Delta t$ at Δt= 10s for all 3 groups (Fig. 4D). We find the mean velocity for groups I, II and III to be $-6 \times 10^{-4} \pm 5 \times 10^{-4} \mu\text{ms}^{-1}$, $-2 \times 10^{-4} \pm 3 \times 10^{-4} \mu\text{ms}^{-1}$ and $1 \times 10^{-3} \pm 3 \times 10^{-4} \mu\text{ms}^{-1}$, respectively, and the skew of -0.75, 0.08 and 0.62, respectively. Our data shows that the skew of the $\Delta d/\Delta t$ distribution systematically changes from group III to II to I, from positive to negative values. Moreover, we find that $\Delta d/\Delta t$ distribution for nucleoli in group I, which are the ones closest to one another, is significantly biased towards negative values. This implies that nucleoli in group I experience a net motion towards one another. To assess the statistical significance of this observation, we generated 10^4 Gaussian samples with the same number of datapoints and variance as in Fig. 4D. We find that skew of data in group I in Fig. 4D is indeed statistically significant, with its value being 3σ away from the mean of the skew of the Gaussian samples ($p-$value of 3×10^{-3}, Fig. S12).

These results are consistent with our observations in Fig. 3H, which showed a decrease in the relative chromatin density between nucleoli with their proximity to each other. The reduction of chromatin density between nucleoli and nucleolar motion towards each other is further consistent with a depletion attraction (50). A decrease in chromatin density might reduce the mechanical resistance to the nucleolar motion in the space between the nucleolar pair. In particular, a reduction in heterochromatin concentration may lead to a reduction of the elastic modulus and viscosity of chromatin in the intranucleolar space (46).

3.5 An Effective Model of Anomalous Nucleolar Coalescence *in Vivo*

We hypothesize that chromatin depletion in the space between two nucleoli prior to their coalescence may effectively cause an attractive depletion interaction between the two nucleoli. Indeed, an attractive force affecting nucleoli prior to coalescence could influence the kinetics of the nucleolar coalescence and possibly lead to the observed anomalous volume distribution $P(V) \sim V^{-1}$ of human nucleoli (Fig. 1). We test this hypothesis by simulating a system of droplets, which experience an attractive force.

To this end, we employ a simple simulation scheme, which is similar to the simulations in (34, 36, 42). Specifically, the simulation consists of a set of 10 nucleoli within a box with periodic boundary conditions, which represents a nucleus. Nucleoli are initialized with small volumes, corresponding to a volume fraction $\phi = 5\%$ of the simulation box (see *Materials and Methods*, Section 2.7). We perform in parallel 100 independent simulations, the results of which we then combine to construct the probability distribution of nucleolar volumes. This resembles the situation seen in experiments, as each human nucleus contains 10 nucleoli at the beginning of the cell cycle. The droplet positions over time are evolved following a subdiffusive fractional Gaussian motion, although we found that our results are insensitive to the absolute value of the subdiffusive exponent of this motion. Upon contact, two droplets coalescence forming one larger droplet, volume of which equals to the sum of the two coalescing droplets. The new droplet randomly "inherits" one of its parents' subdiffusive paths that were generated at the start of the simulation. Finally, we also allow for a pairwise, exponentially screened attractive force:

$$\vec{F}_a = A e^{-r/(\sigma l)} \hat{r} \ , \tag{2}$$

where A and σ are parameters in the model, l is the radius of the larger of the two droplets, and $\vec{r}$ is the relative position of the two droplets. To speed up calculations, $\vec{F}_a$ is cut off to 0 if the droplets are further than $l\sigma$ apart from each other.

First, we sought to reproduce the nucleolar volume distribution found in absence of any interactions, i.e. $P(V) \sim V^{-1.5}$ (34). To do so, we continuously injected new small particles at each time point as prescribed in the original work, and we systematically removed any particles that get too large (i.e. their size is > 1/10 of the box size) to allow the system to reach steady-state. Fig. 5A shows 3 snapshots from such a simulation. An example of an entire simulation can be viewed in Movie S1.

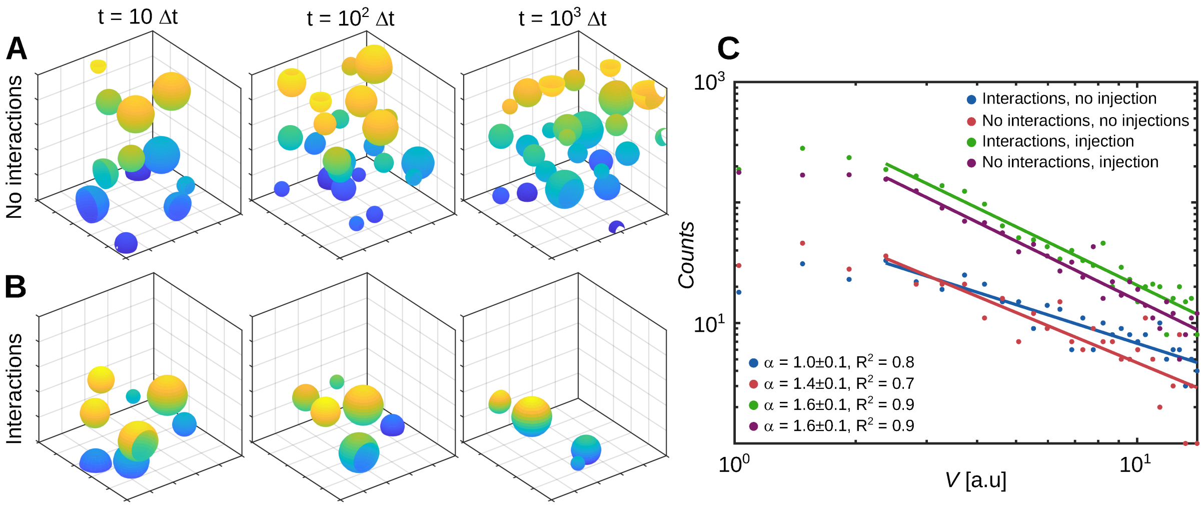

Figure 5: Simulations of nucleolar coalescence for nucleoli with and without interactions. (A) Simulation of nucleoli coalescing in the absence of any interactions and an injection rate of 1, with 3 time points showing droplet coarsening over time. (B) Simulation of nucleoli coalescing in the presence of attractive forces defined by Eq. 2 and no injection, with 3 time points showing droplet coarsening over time. (C) Nucleolar volume distributions obtained for simulations in 4 scenarios: attractive interactions with no injection (*blue*), no interactions or injection (*red)*, both interactions and injection (*green*), and injection with no interactions (*purple*). The distributions in each case were fit to a power-law $P(V) \sim V^{-\alpha}$ by performing linear regression on the log-log histogram of the data, with fits shown as solid lines. In each case, the data were collected over 100 parallel simulations with 10 initial droplets. To ensure that in the absence of particle injection, the interactions make a significant difference, we compared the (*blue* and *red*) volume distributions with a two-sample Kolmogorov-Smirnov test, yielding a $p-$value of 5×10^{-3}.

In these simulations, we set $A = 0$, thus removing any pairwise forces. The system quickly reaches a steady-state with a volume distribution of $P(V) \sim V^{-1.5}$, as shown in Fig. 5C.

Next, we stop the injection of particles, and turn on the pairwise attractive forces in our simulation. The parameters were set to $\sigma = 10$ and $A = 100$ in arbitrary units. This leads to the dynamics seen in Fig. 5B, and the resulting volume distribution $P(V) \sim V^{-1}$ shown in Fig. 5C. An example of an entire simulation including attractive interactions can be viewed in Movie S2. Both power laws shown in Fig. 5C were found to be robust over a wide range of parameters (see *Supplemental Information*, Section 2). The effective diffusion coefficient D of the droplets is assumed to scale inversely with the droplet radius R as given by the Stokes-Einstein relation $D \sim 1/R$ (53). Thus, the step size of larger particles becomes smaller. In our simulations we remove particles once they get too large to avoid all droplets quickly converging into a single droplet state. This leads to a decrease in total particle volume with time, yet the scaling exponent of the volume distribution is still conserved. We find that the distribution quickly reaches $P(V) \sim V^{-1}$ scaling (Fig. 5C). Furthermore, to check that the specific combination of attractive interactions and no particle injection was needed to obtain this anomalous exponent, we also performed simulations with both attractive interactions and particle injection, as well as simulations where neither effect is present. The former yields scaling of $P(V) \sim V^{-1.6}$, the latter yields scaling of $P(V) \sim V^{-1.4}$. Thus, the scaling of $P(V) \sim V^{-1}$ is unique for the case accounting for attractive interactions, but no injection (for p-values, see Fig. 5C).

Overall, we conclude that the anomalous nucleolar volume distribution found in human nuclei can be reproduced with an addition of a pairwise attractive interaction between nucleoli immediately prior to their coalescence. We choose to screen this attractive force, as our experiments revealed that changes in nucleolar dynamics and chromatin density in between them occur only immediately prior to the nucleolar coalescence. Of course, this is not a complete model of the physics of nucleolar coalescence, however, it suggests that such an attractive force is indeed *sufficient* to explain the observed nucleolar volume distribution. In the light of our experimental observations, we speculate that nucleoli may indeed experience an attraction due to an effective depletion interaction, caused by chromatin depletion in the space between two nucleoli prior to their coalescence.

4 DISCUSSION & CONCLUSIONS

Our results provide new mechanistic insights into the process of nucleolar droplet coarsening in human cells. In previous works, individual nucleoli were studied and identified to be liquid droplets embedded in the chromatin-nucleoplasm solution, and the short-time kinetics of their coalescence was used to probe rheology of their environment (32, 34). However, the aggregate

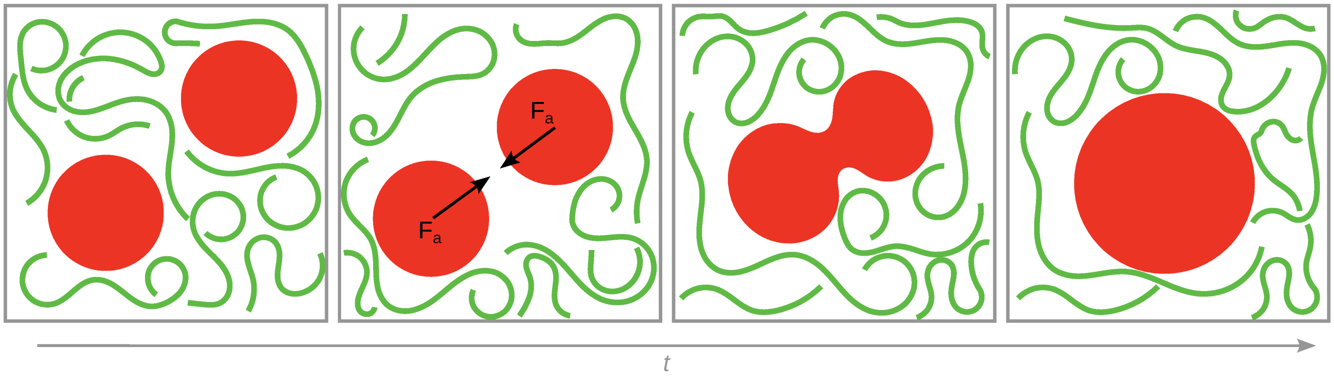

Figure 6: Schematic of a possible physical mechanism contributing to the anomalous coalescence of nucleoli. Two nucleoli (*red*) are immersed in chromatin (*green*). At certain distance from each other, chromatin concentration in the space between the two nucleoli decreases, with heterochromatin at the inner boundary dissolving and chromatin moving out of the space between the nucleoli. This leads to a higher chromatin concentration around the nucleoli, and thus may effectively lead to an attractive depletion force F_a between the nucleoli due to an increase of the osmotic pressure of the surrounding chromatin solution. This attractive interaction could allow nucleoli to come together faster and undergo coalescence, leading to the anomalous nucleolar volume distribution $\sim V^{-1}$.

behavior of this embedded nucleolar phase and the volume distribution of its droplets remained an open question (33). We have successfully reproduced the previously identified anomalous volume distribution of nucleoli $P(V) \sim V^{-1}$, moreover, we revealed it persists during the entire cell cycle. This suggests that the mechanism behind this anomaly is likely of physical origin, which we sought to investigate by examining the detailed mechanics of droplet pairs during their coalescence. Other processes such as Ostwald ripening may also contribute to the observed nucleolar volume distribution, but our data indicates that for the first 15h of the cell cycle coalescence dominates the nucleolar coarsening. At later times, we find a small increase in volume of non-fusing nucleoli ($\sim$ 15%), however, the nucleolar volume scaling of $P(V) \sim V^{-1}$ remains unchanged. Thus, while we do not rule out contribution of other processes to nucleolar coarsening, especially later in the cell cycle, our data suggests that coalescence is the dominant mechanism of nucleolar coarsening in human cells.

To reveal the physical origin of the anomalous volume distribution of human nucleoli, we asked whether dynamic behavior of chromatin may contribute to the rate of droplet coalescence, given that chromatin is a known constraint on nucleolar dynamics (32, 37). To this end, we studied chromatin motions and density between and around nucleoli, as well as nucleolar motions. Indeed, we find that chromatin flows and density in the space between nucleoli as well as nucleolar motions change as the nucleoli approach each other before coalescence. The heterochromatin layer on the nucleolar surface depletes in the space between the nucleoli, once they get in close proximity, consistent with chromatin efflux from the space between nucleoli. Specifically, we find that chromatin density between nucleoli and nucleolar motions are strongly correlated with their distance from each other. While the chromatin density decreases with decreasing nucleolar distance, the nucleolar mobility increases and shows a strong bias for nucleolar motions towards each other. These observations are consistent with the dynamical signatures of a depletion attraction (50). Fig. 6 shows the cartoon of the proposed physical mechanism: When two nucleoli are in close proximity, chromatin becomes depleted in the space between them. This leads to an attractive force between nucleoli, due to a decrease of osmotic pressure between nucleoli.

Such an attractive internucleolar force may lead to a facilitated coalescence, i.e. coalescence not primarily driven by diffusion. We modeled this force as a simple decaying exponential attraction between droplets in our stochastic simulations of nucleolar droplets and observed the power-law of the resulting droplet volume distribution changes from $P \sim V^{-1.5}$ for diffusion-limited case to the anomalous $P \sim V^{-1}$, when attractive forces act between the droplets. Such an attractive force effectively leads to more large droplets present. In human cells, it may be beneficial to aid growth of their nucleoli, as larger volumes may improve the droplets' ability to serve both as a chemical reactor and as a quality control compartment for misfolded proteins (54, 55). We also note that this depletion effect may be one of several processes facilitating attractive interactions between nucleoli prior to their coalescence. For example, interactions of HP1 condensates engulfing the heterochromatin at the nucleolar surface could also be involved, and remain to be explored in future studies.

It is worth considering what properties of nucleoli in *X. Laevis* oocytes versus human cells, would lead to such different distributions in their nucleolar volumes. As mentioned earlier, a combination of two effects leads to a scaling exponent of -1.5: a steady stream of injected small droplets, and no interactions between the diffusing droplets. Both of these can be indeed mapped to properties of nucleoli in *X. Laevis* oocytes. Specifically, the large number of nucleoli in the frog nuclei presents effectively a steady stream of droplets accessible to the coarsening process (34). In other words, in any given small region of the nucleus, new droplets become available at a steady rate. Meanwhile, the lack of internuclolar attractive interactions may be explained by the fact that chromatin in *X. Laevis* oocyte nuclei is present at very low concentration due to the large volume of the germinal vesicle (35). Moreover, its chromatin is organized in the form of "lampbrush chromosomes", a tightly-packed structure, which does not permeate the nucleus in the same way as human interphase chromatin does (56, 57). Therefore, it is likely that the mechanism of chromatin-aided nucleolar coalescence identified in this work in human cells could not take place in the frog egg nuclei. Instead, it was suggested that actin filaments help to hold the nucleoli spatially distributed in the large volume of the frog egg germinal vesicle (34). Finally, a recent study found that the nature of the droplet size distribution (exponential vs. power-law) is given by the relative rates of nucleation and coalescence, with higher rates of nucleation leading to exponential distribution and higher rates of coalescence to power-law distributions (42). Our findings of human nucleoli *in vivo* following a power-law distribution are consistent with the coalescence dominating the nucleolar volume distributions.

In summary, we have identified a possible physical mechanism of chromatin-faciliated nucleolar coalescence, where chromatin aids in both the approach and coalescence of nucleolar droplets. Such mechanism could explain the anomalous coarsening of human nucleoli. Of course, our proposed mechanism is likely only one of many contributing factors, considering the complexity of the studied system, ranging from the finite size of the human nucleus, the small number of nucleoli in human cells, presence of active ATP-dependent processes in both the nucleus and nucleolus, viscoelasticity of the chromatin surrounding human nucleoli, to large-scale coherent motions of chromatin in the cell nucleus (19, 21, 40, 58). Investigating effects of these processes on the nucleolar coarsening may provide further insights into the physics of nuclear organization, contributing to our understanding of the human cell nucleus in health and disease.

5 AUTHOR CONTRIBUTIONS

The project was designed by A.Z., experiments were performed by G.A., C.M.C. and A.W., simulations were carried out by I.E., data analysis was performed by G.A., C.M.C., T.C., I.E., Y.Y., A.W. and A.Z., the manuscript was written by G.A., T.C., I.E. and A.Z.

6 DECLARATION OF INTERESTS

The authors declare no competing interests.

7 ACKNOWLEDGMENTS

This research was supported in part by the NSF Grants CAREER PHY-1554880, CMMI-1762506, PHY-2210541, NYU MRSEC DMR-1420073 and the NIH Grant R01-GM145924. DCS calculations were carried out using New York University (NYU) High Performance Computing cluster.

REFERENCES

1. Hutchison, H., and D. Sutherland, 1965. An open-structured random solid. *Nature* 206:1036–1037.
2. Jayanth, C., and P. Nash, 1989. Factors affecting particle-coarsening kinetics and size distribution. *J. Mat. Sci.* 24:3041–3052.
3. Berry, J., C. P. Brangwynne, and M. Haataja, 2018. Physical principles of intracellular organization via active and passive phase transitions. *Rep. Prog. Phys.* 81:046601.
4. Friedlander, S. K., et al., 2000. Smoke, dust, and haze, volume 198. Oxford University Press New York.
5. Uversky, V. N., and D. Eliezer, 2009. Biophysics of Parkinson's disease: structure and aggregation of α-synuclein. *Curr. Protein Pept.* 10:483–499.
6. Chiti, F., and C. M. Dobson, 2017. Protein misfolding, amyloid formation, and human disease: a summary of progress over the last decade. *Annu. Rev. Biochem.* 86:27–68.
7. Fuchs, N., and A. Sutugin, 1971. High-dispersed aerosols. *In* Topics in current aerosol research, Elsevier, 1.
8. Witten, T. A., and L. M. Sander, 1983. Diffusion-limited aggregation. *Phys. Rev. B* 27:5686.
9. Weitz, D., and M. Lin, 1986. Dynamic scaling of cluster-mass distributions in kinetic colloid aggregation. *Phys. Rev. Lett.* 57:2037.
10. Family, F., and P. Meakin, 1989. Kinetics of droplet growth processes: Simulations, theory, and experiments. *Phys. Rev. A* 40:3836.
11. Meakin, P., 1990. Diffusion-limited droplet coalescence. *Phys. A: Stat. Mech. Appl.* 165:1–18.

12. Yao, J. H., K. Elder, H. Guo, and M. Grant, 1993. Theory and simulation of Ostwald ripening. *Phys. Rev. B* 47:14110.

13. Paulsen, J. D., J. C. Burton, and S. R. Nagel, 2011. Viscous to inertial crossover in liquid drop coalescence. *Phys. Rev. Lett.* 106:114501.

14. Paulsen, J. D., R. Carmigniani, A. Kannan, J. C. Burton, and S. R. Nagel, 2014. Coalescence of bubbles and drops in an outer fluid. *Nat. Commun.* 5:3182.

15. Smoluchowski, M., 1927. Drei Vorträge über Diffusion, Brownsche Molekularbewegung und Koagulation von Kolloidteilchen. *Pisma Mariana Smoluchowskiego* 2:530–594.

16. Van Dongen, P., and M. Ernst, 1985. Dynamic scaling in the kinetics of clustering. *Phys. Rev. Lett.* 54:1396.

17. Huber, G., 1991. Scheidegger's rivers, Takayasu's aggregates and continued fractions. *Phys. A: Stat. Mech. Appl.* 170:463–470.

18. Takayasu, H., I. Nishikawa, and H. Tasaki, 1988. Power-law mass distribution of aggregation systems with injection. *Phys. Rev. A* 37:3110.

19. Hyman, A. A., C. A. Weber, and F. Jülicher, 2014. Liquid-liquid phase separation in biology. *Annu. Rev. Cell Dev. Biol.* 30:39–58.

20. Alberti, S., A. Gladfelter, and T. Mittag, 2019. Considerations and challenges in studying liquid-liquid phase separation and biomolecular condensates. *Cell* 176:419–434.

21. Zidovska, A., 2020. The rich inner life of the cell nucleus: dynamic organization, active flows, and emergent rheology. *Biophys. Rev.* 12:1093–1106.

22. Alberts, B., A. Johnson, J. Lewis, D. Morgan, M. Raff, K. Roberts, and P. Walter, 2014. Molecular Biology of the Cell. Garland Science.

23. Montanaro, L., D. Treré, and M. Derenzini, 2008. Nucleolus, ribosomes, and cancer. *Am. J. Pathol.* 173:301–310.

24. Boulon, S., B. J. Westman, S. Hutten, F.-M. Boisvert, and A. I. Lamond, 2010. The nucleolus under stress. *Mol. Cell* 40:216–227.

25. McClintock, B., 1934. The relation of a particular chromosomal element to the development of the nucleoli in *Zea Mays*. *Cell Tissue Res.* 21:294–326.

26. Ritossa, F., and S. Spiegelman, 1965. Localization of DNA complementary to ribosomal RNA in the nucleolus organizer region of *Drosophila Melanogaster*. *Proc. Natl. Acad. Sci. U.S.A.* 53:737–745.

27. Wallace, H., and M. Birnstiel, 1966. Ribosomal cistrons and the nucleolar organizer. *Biochim. Biophys. Acta* 114:296–310.

28. Anastassova-Kristeva, M., 1977. The nucleolar cycle in man. *J. Cell Sci.* 25:103–110.

29. Floutsakou, I., S. Agrawal, T. T. Nguyen, C. Seoighe, A. R. Ganley, and B. McStay, 2013. The shared genomic architecture of human nucleolar organizer regions. *Genome Res.* 23:2003–2012.

30. Amenta, P. S., 1961. Fusion of nucleoli in cells cultured from the heart of *Triturus viridescens*. *Anat. Rec.* 139:155–165.

31. Sullivan, G. J., J. M. Bridger, A. P. Cuthbert, R. F. Newbold, W. A. Bickmore, and B. McStay, 2001. Human acrocentric chromosomes with transcriptionally silent nucleolar organizer regions associate with nucleoli. *EMBO J.* 20:2867–2877.

32. Caragine, C. M., S. C. Haley, and A. Zidovska, 2018. Surface fluctuations and coalescence of nucleolar droplets in the human cell nucleus. *Phys. Rev. Lett.* 121:148101.

33. Caragine, C. M., S. C. Haley, and A. Zidovska, 2019. Nucleolar dynamics and interactions with nucleoplasm in living cells. *eLife* 8:e47533.

34. Brangwynne, C. P., T. J. Mitchison, and A. A. Hyman, 2011. Active liquid-like behavior of nucleoli determines their size and shape in *Xenopus Laevis* oocytes. *Proc. Natl. Acad. Sci. U.S.A.* 108:4334–4339.

35. Gall, J. G., C. Murphy, H. Gao, et al., 2004. Structure in the amphibian germinal vesicle. *Exp. Cell Res.* 296:28–34.

36. Lee, D. S., N. S. Wingreen, and C. P. Brangwynne, 2021. Chromatin mechanics dictates subdiffusion and coarsening dynamics of embedded condensates. *Nat. Phys.* 17:531–538.

37. Qi, Y., and B. Zhang, 2021. Chromatin network retards nucleoli coalescence. *Nat. Commun.* 12:1–10.

38. Zhang, Y., D. S. Lee, Y. Meir, C. P. Brangwynne, and N. S. Wingreen, 2021. Mechanical frustration of phase separation in the cell nucleus by chromatin. *Phys. Rev. Lett.* 126:258102.

39. Chu, F.-Y., S. C. Haley, and A. Zidovska, 2017. On the origin of shape fluctuations of the cell nucleus. *Proc. Natl. Acad. Sci. U.S.A.* 114:10338–10343.

40. Zidovska, A., D. A. Weitz, and T. J. Mitchison, 2013. Micron-scale coherence in interphase chromatin dynamics. *Proc. Natl. Acad. Sci. U.S.A.* 110:15555–15560.

41. Courant, R., F. John, A. A. Blank, and A. Solomon, 1965. Introduction to calculus and analysis, volume 1. Springer.

42. Lee, D. S., C.-H. Choi, D. W. Sanders, L. Beckers, J. A. Riback, C. P. Brangwynne, and N. S. Wingreen, 2023. Size distributions of intracellular condensates reflect competition between coalescence and nucleation. *Nat. Phys.* 19:586–596.

43. Stoev, S. A. FFT Fractional Gaussian Noise. `http://dept.stat.lsa.umich.edu/~sstoev/code/ffgn.m`. [Online; accessed April 11 2023].

44. Perrin, E., R. Harba, R. Jennane, and I. Iribarren, 2002. Fast and exact synthesis for 1-D fractional Brownian motion and fractional Gaussian noises. *IEEE Signal Process. Lett.* 9:382–384.

45. Saintillan, D., M. J. Shelley, and A. Zidovska, 2018. Extensile motor activity drives coherent motions in a model of interphase chromatin. *Proc. Natl. Acad. Sci. U.S.A.* 115:11442–11447.

46. Eshghi, I., J. A. Eaton, and A. Zidovska, 2021. Interphase chromatin undergoes a local sol-gel transition upon cell differentiation. *Phys. Rev. Lett.* 126:228101.

47. Padeken, J., and P. Heun, 2014. Nucleolus and nuclear periphery: velcro for heterochromatin. *Curr. Opin. Cell Biol.* 28:54–60.

48. Guetg, C., and R. Santoro, 2012. Formation of nuclear heterochromatin: the nucleolar point of view. *Epigenetics* 7:811–814.

49. Kimura, H., and P. R. Cook, 2001. Kinetics of core histones in living human cells: little exchange of H3 and H4 and some rapid exchange of H2B. *J. Cell Biol.* 153:1341–1354.

50. Israelachvili, J., 1992. Ontermolecular and Surface Forces. Academic Press.

51. Mao, Y., M. Cates, and H. Lekkerkerker, 1995. Depletion force in colloidal systems. *Physica A: Statistical Mechanics and its Applications* 222:10–24.

52. Tuinier, R., J. Rieger, and C. De Kruif, 2003. Depletion-induced phase separation in colloid–polymer mixtures. *Advances in colloid and interface science* 103:1–31.

53. Einstein, A., 1905. Über die von der molekularkinetischen Theorie der Wärme geforderte Bewegung von in ruhenden Flüssigkeiten suspendierten Teilchen. *Ann. Phys.* 4.

54. Boisvert, F.-M., S. van Koningsbruggen, J. Navascués, and A. I. Lamond, 2007. The multifunctional nucleolus. *Nat. Rev. Mol. Cell Biol.* 8:574.

55. Frottin, F., F. Schueder, S. Tiwary, R. Gupta, R. Körner, T. Schlichthaerle, J. Cox, R. Jungmann, F. Hartl, and M. Hipp, 2019. The nucleolus functions as a phase-separated protein quality control compartment. *Science* 365:342–347.

56. Gall, J. G., C. Murphy, H. G. Callan, et al., 1991. Lampbrush chromosomes. *In* Methods Cell Biol., Elsevier, volume 36, 149–166.

57. Patel, S., N. Novikova, B. Beenders, C. Austin, and M. Bellini, 2008. Live images of RNA polymerase II transcription units. *Chromosome Res.* 16:223–232.

58. Zidovska, A., 2020. The self-stirred genome: large-scale chromatin dynamics, its biophysical origins and implications. *Curr. Opin. Genet. Dev.* 61:83–90.